Journal of Colloid and Interface Science 533 (2019) 319–332

Contents lists available at ScienceDirect

Journal of Colloid and Interface Science

journal homepage: www.elsevier.com/locate/jcis

Composite photocatalyst, tetragonal lead bismuth oxyiodide/bismuth oxyiodide/graphitic carbon nitride: Synthesis, characterization, and photocatalytic activity

Ai-Hsuan Lee, Yi-Chuen Wang, Chiing-Chang Chen *

Department of Science Education and Application, National Taichung University of Education, Taichung 403, Taiwan

GRAPHICAL ABSTRACT

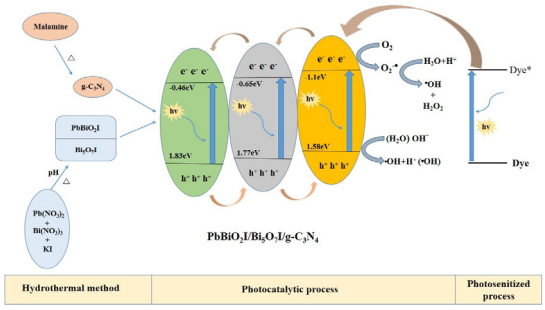

ARTICLE INFO

Article history:
Received 5 May 2018
Revised 16 July 2018
Accepted 5 August 2018
Available online 6 August 2018

Keywords:
$PbBiO_2I$
Bi_5O_7I
g-C_3N_4
Composites
Photocatalytic

ABSTRACT

Semiconductor photocatalysts that are robust and galvanized by visible light have been increasingly sought after, with lead bismuth oxyhalide ($PbBiO_2X$)—which constitutes a perovskite-like semiconductor—receiving vast attention recently. We noted, after a relevant literature survey, that tetragonal lead bismuth oxyiodide/bismuth oxyiodide/graphitic carbon nitride (*t*-$PbBiO_2I/Bi_5O_7I$/g-C_3N_4)-supported crystal violet (CV) dye photocatalytic degradation under irradiation with visible light has yet to be reported. The current study provides the report of *t*-$PbBiO_2I/Bi_5O_7I$/g-C_3N_4 composite isolation and characterization realized through field-emission scanning electron microscopy–energy-dispersive spectroscopy, X-ray diffraction, high-resolution X-ray photoelectron spectroscopy, transmission electron microscopy, photoluminescence spectroscopy, Brunauer–Emmett–Teller analysis, Fourier-transform infrared spectroscopy, and ultraviolet–visible diffuse reflectance spectroscopy. Catalytic performance observation revealed that using *t*-$PbBiO_2I/Bi_5O_7I$/g-C_3N_4 resulted in an optimal reaction rate constant of 0.3518 h^{-1}, a derivation exceeding the derivations for the photocatalysts *t*-$PbBiO_2I$, Bi_5O_7I, g-C_3N_4, and *t*-$PbBiO_2I/Bi_5O_7I$ by 15, 6.6, 13.1, and 1.4 times, respectively. As demonstrated by the quenching effects associated with diverse scavengers, the electron paramagnetic resonance results revealed reactive O_2^- to have a major role in the CV dye degradation. The paper proposes and also describes possible photodegradation mechanisms. The method that was realized in this study is valuable for $PbBiO_2I/Bi_5O_7I$/g-C_3N_4 synthesis and CV dye photocatalytic degradation for future applications in environmental pollution regulation.

* Corresponding author.
E-mail address: ccchen@mail.ntcu.edu.tw (C.-C. Chen).

https://doi.org/10.1016/j.jcis.2018.08.008
0021-9797/

1. Introduction

Toxic chemicals are known to exert hazardous influences on living beings and on the environment; therefore, extracting these chemicals from wastewater is among the most vital facets of modern strategies of controlling pollution. Countries are facing increasingly severe problems of environmental pollution and energy demands; photocatalysis constitutes an adequate technology for addressing these problems, and it is integral in pollutant degradation as well as in solar energy conversion [1]. A photocatalyst of low cost and exhibiting environmental robustness is crucial for executing photocatalysis in practice [2].

Scholars have broadly probed structure compounds that are based on Bi, are layered, and are part of the Aurivillius family—which include BiOX (X = Cl, Br, I) [3,4], $Bi_4Ti_3O_{12}$ [5], and $BiVO_4$ [6]—for application as strongly efficient photocatalysts; this is because such compounds exhibit a distinct layered structure and high catalytic activity. The levels of Bi 6s and O 2p are considered to engender a hybridized valence band (VB) that is predominantly dispersed, a property that advances photogenerated hole mobility and the oxidation reaction, consequently inducing photogenerated electron–hole pair segregation and subsequent photocatalytic efficiency augmentation [7]. The structures of numerous inorganic materials are determined to be modular, with different functions being supervised by individual units. $[Bi_2O_2]^{2+}$ slabs that exhibit an α-PbO-type structure, in addition to possessing simple halide layers, constitute effective spacers in certain functional materials that are layered [8]. Studies on the mechanisms associated with the divergent photocatalytic activities of lead bismuth oxyhalide ($PbBiO_2X$)-type materials that are layered (X = Cl, Br, I) have mainly discussed electronic reasons [9-14]. However, an expounding of the photocatalytic properties of the compounds should also consider crystal-chemical arguments. The oxides' crystal structures, optic, and redox properties possibly collectively explain their divergent catalytic activities. A common property among all the discussed solid materials is related to their crystallization in a layered structure. The materials possess halide-layer-separated covalent metal oxygen layers $[PbBiO_2]^+$ stacked along [0 0 1]. The crystal surface can be assumed as comprising layers of metal oxygen; in other words, the (0 0 1) surfaces are expected to be formed by the metal atoms. Concerning bismuth compounds, lead and bismuth were statistically determined to occupy the metal position at a 1:1 ratio [15]. The $PbBiO_2I$ [16], $PbBiO_2Br$ [9], and $PbBiO_2Cl$ [10] band gap values have been reported to be 2.39, 2.47, and 2.53 eV, respectively. These values suggest that the gaps determined for all the aforementioned semiconductors exist in the visible-light region; hence, they can be utilized in photocatalytic reaction catalysis.

Studies have reported that heterojunctions associated with $PbBiO_2X$—which include $PbBiO_2I$/PbO [17], MoS_2/$PbBiO_2I$ [18], $PbBiO_2Br$/BiOBr [9], $PbBiO_2Br$/g-C_3N_4 [19], $PbBiO_2Br$/UiO-66-NH_2 [20], AgBr/Ag/$PbBiO_2Br$ [21], and $PbBiO_2Br$/$NbSe_2$ [22]—exhibit improved photocatalytic efficiency. Accordingly, an ion exchange reaction that partly transforms $PbBiO_2Br$ into $NbSe_2$ through a direction that is thermodynamically favored is a feasible concept; doing so enables the component ions to engage in exchange processes with the incoming species [23], consequently yielding a $PbBiO_2Br$/$NbSe_2$ heterojunction. As shown in Table 1, heterojunctions associated with $PbBiO_2X$ has obtained remarkable interests in recent years because of their suitable band gaps, stability, and relatively superior photocatalytic activities [9,11,17-21]. It is found that the $PbBiO_2X$ composite shows higher photocatalytic activities than $PbBiO_2X$ for the photocatalytic degradation of organic compound do.

We noted, after a relevant literature survey, that *t*-$PbBiO_2I$/Bi_5O_7I/g-C_3N_4–containing nanocomposite semiconductors have yet to be reported. The current study thus provides the demonstration of *t*-$PbBiO_2I$/Bi_5O_7I/g-C_3N_4 composite preparation through the execution of a template-free hydrothermal method. Crystal violet (CV) degradation was realized in this study in aqueous solution under irradiation by visible light; the study also probed the corresponding photocatalytic activities of the produced *t*-$PbBiO_2I$/Bi_5O_7I/g-C_3N_4 products.

2. Experimental details

2.1. Materials

Crystal violet dye (CV; 99%, Tokyo Kasei Kogyo Co.), 2-hydroxybenzoic acid (HBA; salicylic acid, 99%, Katayama), Bi$(NO_3)_3{\cdot}5H_2O$ (98%, Sigma-Aldrich), Pb$(NO_3)_2{\cdot}H_2O$ (99%, Katayama), ammonium oxalate (AO, 99%, Osaka), isopropanol (IPA, 99.9%, Merck), sodium azide (SA, 99.5%, Sigma-Aldrich), and *p*-benzoquinone (BQ, 98%, Alfa Aesar) were purchased and applied in this study as obtained.

2.2. Analytical methods and instruments

Segregation and identification processes were completed using a liquid chromatography/mass spectrometry (LC/MS) apparatus (Waters ZQ) comprising an autosampler, binary pump, micromass detector, and photodiode array detector. HPLC-MS quantified the residual dye amount in each reaction cycle [24].

A microscope (JEOL-2010; 200-kV acceleration voltage) was employed in this study for executing field-emission transmission electron microscopy (FE-TEM), selected-area electron diffraction, high-resolution TEM (HR-TEM), and energy-dispersive spectroscopy (EDS). Furthermore, a JEOL JSM-7401F device (15-kV acceleration voltage) was employed in this study for FE scanning electron microscopy (FE-SEM)-EDS. A Micrometrics Gemini automated system was also applied to measure the samples' Brunauer–Emmett–Teller (BET) specific surface areas (S_{BET}), with the adsorbate being nitrogen gas that was at liquid nitrogen temperature. A MAC Science MXP18 apparatus involving Cu-Kα radiation and operated at 40 kV and 80 mA was utilized for X-ray diffraction (XRD). Moreover, 15-kV Al-Kα radiation was applied. A ULVAC-PHI system was applied to execute HR X-ray photoelectron spectroscopy (HR-XPS).

2.3. Synthesis of t-$PbBiO_2I$/Bi_5O_7I and g-C_3N_4

First, Pb$(NO_3)_2{\cdot}H_2O$ (1, 3, and 5 mmol) and Bi$(NO_3)_3{\cdot}5H_2O$ (3 mmol) were mixed in a flask that measured 50 mL, followed by the addition of 15 mL of 1 M HNO_3. Next, 5 M NaOH was introduced on a dropwise basis under continuous stirring to adjust the pH within 1–13; subsequently, upon white precipitate formation, 1 mL of 1 M KI was also introduced on a dropwise basis. The next step entailed subjecting the solution to 30-min vigorous stirring; of this derived solution, 24 mL was moved into an autoclave (30 mL) that was lined with Teflon, with the autoclave being subjected to heating up to 100–150 °C for 12 h, followed by natural cooling to room temperature. Through filtration, the derived solid precipitate was collected; deionized water and ethanol were next applied to wash the derived precipitate to remove any possible ionic species, after which the precipitate was dried overnight at 60 °C. Composites of $PbBiO_2I$/Bi_5O_7I were realized using the relevant Pb$(NO_3)_2{\cdot}H_2O$/Bi$(NO_3)_3{\cdot}5H_2O$ molar ratio (1:3, 3:3, or 3:5), pH value, temperature, and reaction time (Supplementary Table S1); for the as-prepared samples, the formulated designations ranged from B3PI-1-100-12 to B3P5I-13-150-12.

Supplementary data associated with this article can be found, in the online version, at https://doi.org/10.1016/j.jcis.2018.08.008.

Table 1
Photocatalytic properties of $PbBiO_2X$ nanocomposite photocatalysts under visible light irradiation.

Composite photocatalyst	Light source	Degradation compounds	Photocatalytic activity	Reference photocatalyst/ photocatalytic activity	Enhancement factor	Reference
t-$PbBiO_2I/Bi_5O_7I$/ g-C_3N_4	150 W Xe arc lamp; λ > 420 nm	1. Crystal violet 2. 2-Hydroxybenzoic acid	1. 95% degradation in 24 h 2. 96% degradation in 12 h	g-C_3N_4: k = 0.0254 h^{-1} *t*-$PbBiO_2I/Bi_5O_7I$: k = 0.2518 h^{-1}	13.1 1.4	This paper
$PbBiO_2I/MoS_2$	300 W Xe lamp; λ > 400 nm	1. Rhodamine B 2. Ciprofloxacin 3. Bisphenol A	1. 99% degradation in 3 h 2. 83% degradation in 6 h 3. 92% degradation in 2 h			[18]
$PbBiO_2Br/BiOBr$	150 W Xe arc lamp; λ > 420 nm	Crystal violet	80.5% degradation in 12 h	$PbBiO_2Br$: k = 0.1024 h^{-1} BiOBr: k = 0.0629 h^{-1}	3 2	[9]
$PbBiO_2Br/g\text{-}C_3N_4$	300 W Xe lamp; λ > 400 nm	1. Rhodamine 2. Tetracycline hydrochloride 3. Bisphenol A	1. 99% degradation in 75 min 2. 43% degradation in 75 min 3. 45% degradation in 5 h	$PbBiO_2Br$ g-C_3N_4		[19]
$PbBiO_2Br$/UiO-66-NH_2	70 W metal halide lamp; λ > 380 nm	Rhodamine B		$PbBiO_2Br$: k = 0.049 min^{-1} UiO-66-NH_2: k = 0.0613 min^{-1}	5 4	[20]
$PbBiO_2Cl/BiOCl$	150 W Xe arc lamp; λ > 420 nm	1. Crystal violet 2. Salicylic acid	1. 99.5% degradation in 72 h 2. 80% degradation in 72 h	BiOCl: k = 0.1303 h^{-1} $PbBiO_2Cl$: k = 0.0918 h^{-1}	2.12 3.01	[11]
$AgBr/Ag/PbBiO_2Br$	300 W Xe arc lamp; λ > 420 nm	1. Rhodamine B 2. Bisphenol A	1. 100% degradation in 25 min 2. 82.3% degradation in 2 h	$PbBiO_2Br$: k = 0.0241 min^{-1}	7.85	[21]
$PbBiO_2I/PbO$	150 W Xe arc lamp; λ > 420 nm	1. Crystal violet 2. 2-Hydroxybenzoic acid	1. 99.5% degradation in 72 h 2. 95% degradation in 72 h	PbO: k = 0.0058 h^{-1} $PbBiO_2I$: k = 0.0386 h^{-1}	20 3	[17]

We synthesized, under atmospheric conditions, g-C_3N_4 powder by directly subjecting melamine to calcination executed in a muffle furnace. A typical sequence in the synthesis procedure is as follows: The first step entailed placing 5 g of melamine in a semi-closed alumina crucible that also had a cover. The subsequent step entailed heating the crucible to 520 °C for 4 h (heating rate: 10 °C/min). After the derived product cooled to room temperature, we obtained g-C_3N_4 powder.

2.4. Synthesis of *t*-$PbBiO_2I/Bi_5O_7I$/g-C_3N_4

This process entailed first mixing *t*-$PbBiO_2I/Bi_5O_7I$ (500–x mg) and g-C_3N_4 (x mg) in a flask that measured 50 mL and then introducing ethylene glycerol (10 mL). For the as-prepared samples, the formulated designations ranged from B3PI-13-x%C3N4-100-12 to B3P5I-4-x%C3N4-150-12 (Table 2). The subsequent step entailed subjecting the solution to 30-min vigorous stirring; of this derived solution, 30 mL was moved into an autoclave (30 mL) that was lined with Teflon, with the autoclave being subjected to heating up to 100–150 °C for 12 h, followed natural cooling to room temperature. Through filtration, the derived solid precipitate was obtained; deionized water and ethanol were next applied to wash the derived precipitate to remove any possible ionic species, after which the precipitate was dried overnight at 60 °C.

2.5. Photocatalytic experiments

An aqueous solution that had been stirred and moved into a flask that measured 100 mL was used for CV irradiation experiments; the aqueous CV suspension (100 mL, 10 ppm) and catalyst powder of a determined amount were moved into a Pyrex flask. The suspension's pH regulation was realized through NaOH or HNO_3 solution addition. For investigating the composites' adsorption–desorption equilibrium, we executed experiments in the dark. The photocatalyst (10 mg) and CV aqueous solution (100 mL) of a determined initial concentration were mixed in a flask that measured 100 mL; the derived mixture was subjected to shaking at a constant temperature in an orbital shaker (100 rpm). Before the execution of irradiation, we subjected the suspension to ca. 30-min magnetic stirring in the dark to realize equilibrium of adsorption and desorption between the applied CV in the experiment and the catalyst surface. Xe arc lamps (150 W) equipped with a 400-nm cutoff filter were employed for irradiation, with the intensity of light set at 30.9 W/m^2 and the distance between the vessel of the reaction and the light source set to 30 cm. We collected, within set irradiation time intervals, a 5-mL aliquot and subjected it to centrifugation for catalyst removal. HPLC-PDA-MS quantified residual dye amount in each reaction cycle.

2.6. Quenching experiments

To measure the effects of active species manifested during the course of the photocatalytic reaction, the study introduced diverse quenchers so as to scavenge the appropriate active species. We examined ·OH, $O_2^{\cdot-}$, h^+, and $^1O_2$, constituting the considered active species, by introducing the following: IPA (1.0 mM), an ·OH quencher [25]; BQ (1.0 mM), an $O_2^{\cdot-}$ quencher [26]; AO (1.0 mM), a h^+ quencher [27]; and SA (1.0 mM), an $^1O_2$ quencher [28] respectively.

3. Results and discussion

3.1. Characterization of as-prepared samples

3.1.1. XRD

Supplementary Fig. S1 illustrates the as-prepared samples' XRD patterns, clearly demonstrating the following composites' existence: *t*-$PbBiO_2I/Bi_5O_7I$, *t*-$PbBiO_2I/Bi_5O_7I$/PbO, *t*-$PbBiO_2I/Bi_5O_7I$/

Table 2
Crystalline phase changes of as-prepared samples under different hydrothermal conditions. ($Pb(NO_3)_2/Bi(NO_3)_3$ = 1/3–5/3, KI = 1 mmol, pH = 1–13, temp = 100–150 °C, time = 12 h).(■: Bi_5O_7I, ●: $Bi_6O_6(OH)_3(NO_3)_3{\cdot}1.5H_2O$, ▲: PbO, ●: *t*-$PbBiO_2I$, ▼: g-$C_3N_4$).

Sample	XRD
B3PI-13-100-12	●■
B3PI-1%C3N4-13-100-12	●■▼
B3PI-5%C3N4-13-100-12	●■▼
B3PI-10%C3N4-13-100-12	●■▼
B3PI-25%C3N4-13-100-12	●■▼
B3PI-50%C3N4-13-100-12	●■▼
B3PI-13-150-12	●■
B3PI-5%C3N4-13-150-12	●■▼
B3PI-10%C3N4-13-150-12	●■▼
B3PI-25%C3N4-13-150-12	●■▼
B3PI-50%C3N4-13-150-12	●■▼
B3P3I-4-100-12	●●■▲
B3P3I-5%C3N4-4-100-12	●●■▲▼
B3P3I-10%C3N4-4-100-12	●●■▲▼
B3P3I-25%C3N4-4-100-12	●●■▲▼
B3P3I-50%C3N4-4-100-12	●●■▲▼
B3P3I-4-150-12	●●■▲
B3P3I-5%C3N4-4-150-12	●●■▲▼
B3P3I-10%C3N4-4-150-12	●●■▲▼
B3P3I-25%C3N4-4-150-12	●●■▲▼
B3P3I-50%C3N4-4-150-12	●●■▲▼
B3P5I-4-100-12	●●■▲
B3P5I-5%C3N4-4-100-12	●●■▲▼
B3P5I-10%C3N4-4-100-12	●●■▲▼
B3P5I-25%C3N4-4-100-12	●●■▲▼
B3P5I-50%C3N4-4-100-12	●●■▲▼
B3P5I-4-150-12	●■▲
B3P5I-5%C3N4-4-150-12	●■▲▼
B3P5I-10%C3N4-4-150-12	●■▲▼
B3P5I-25%C3N4-4-150-12	●■▲▼
B3P5I-50%C3N4-4-150-12	●■▲▼
C_3N_4	▼

$PbO/Bi_6O_6(OH)_3(NO_3)_3{\cdot}1.5H_2O$, $PbO/Bi_6O_6(OH)_3(NO_3)_3{\cdot}1.5H_2O$, $Bi_6O_6(OH)_3(NO_3)_3{\cdot}1.5H_2O$, and *t*-$PbBiO_2I/PbO$. Supplementary Table S2 provides a summary of the derived XRD results. The results revealed the as-prepared samples to comprise the following phases: *t*-$PbBiO_2I$ (JCPDS 38-1007), Bi_5O_7I (JCPDS 40-0548), PbO (JCPDS 085-1287), and $Bi_6O_6(OH)_3(NO_3)_3{\cdot}1.5H_2O$ (JCPDS 053-1038) phases. A hydrothermal reaction's pH has been recognized to considerably influence the products' composition and morphologies. Scholars who have completed controlled experiments aimed at probing the influence of pH on such a reaction have reported pH to be integral in controlling crystal composition and anisotropic growth, in contrast to temperature and molar ratio [24,29]. *t*-$PbBiO_2I/Bi_5O_7I$ was derived at a pH of 13, molar ratios (Pb/Bi) of 1/3, 3/3, and reaction temperatures of 100 and 150 °C.

Fig. 1 and Fig. S2 present the XRD patterns derived for the as-prepared composites; Table 2 provides a summary of the acquired XRD results in this study. The patterns in Fig. 1 clearly demonstrate the following composite's existence: *t*-$PbBiO_2I/Bi_5O_7I/g\text{-}C_3N_4$. This as-prepared sample contained *t*-$PbBiO_2I$ (JCPDS 38-1007), Bi_5O_7I (JCPDS 40-0548), and g-C_3N_4 (JCPDS 87-1526) phases. The XRD results derived for the other samples are summarized in Table 2.

3.1.2. TEM

Fig. 2 displays B3PI-1%C3N4-13-100-12 (*t*-$PbBiO_2I/Bi_5O_7I/g\text{-}C_3N_4$) to comprise long rod, irregular plate, and irregular nanosheet exhibiting different sizes, an observation that is in agreement with the TEM observations. Bi, Pb, I, O, C, and N were also determined to be the constituents of the derived sample, as indicated by the EDS spectrum. As demonstrated by the HR-TEM image that is depicted in Fig. 2(d), this study derived two sets of lattice images revealing d-spacing values of 0.174 and 0.164 nm that were attributed to the (1 0 7) and (9 1 2) planes of *t*-$PbBiO_2I$ and Bi_5O_7I, respectively; this observation was noted in this study to agree strongly with the results derived from XRD. The results suggest *t*-$PbBiO_2I/Bi_5O_7I/g\text{-}C_3N_4$ phase construction in the derived composites, which are beneficial for photoinduced carrier segregation, engendering high levels of photocatalytic activity.

3.1.3. XPS

Fig. 3 presents the *t*-$PbBiO_2I/Bi_5O_7I/g\text{-}C_3N_4$ composites' Pb 4f, Bi 4f, I 3d, O 1s, C 1s, and N 1s XPS spectra, with the transition peaks associated with the orbitals of Bi 4f, Pb 4f, O 1s, I 3d, and C 1s, and N 1s indicating Bi, Pb, O, I, C, and N to be the constituents of the derived catalysts. Table S3 summarized the peak energy and full width at half maximum (FWHM) of Pb 4f, Bi 4f, I 3d, O 1s, C 1s, and N 1s XPS spectra which has fitted by the Gaussian function, respectively. Fig. 3(b) indicates the spectra derived for Pb 4f to be deconvoluted into peaks at 137.2- and 138.2-eV binding energies, ascribed to Pb $4f_{7/2}$, which could be attributed to Pb existing in a divalent oxidation state [30]. Chen et al. determined the $PbBiO_2Cl$ particle size to be possibly correlated with discernible

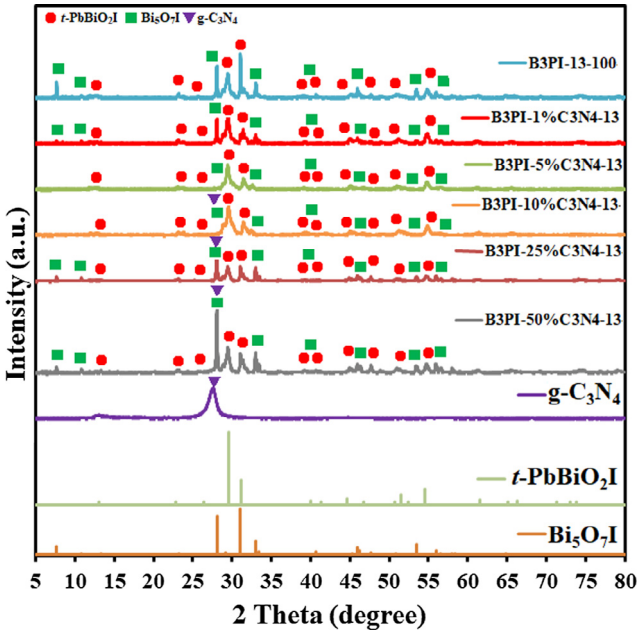

Fig. 1. XRD patterns of as-prepared samples by the hydrothermal autoclave method. (Molar ratio $Pb(NO_3)_2/Bi(NO_3)_3$ = 1/3 mmol/mmol, KI = 1 mmol, pH = 13, reaction temperature = 150 °C, reaction times = 12 h).

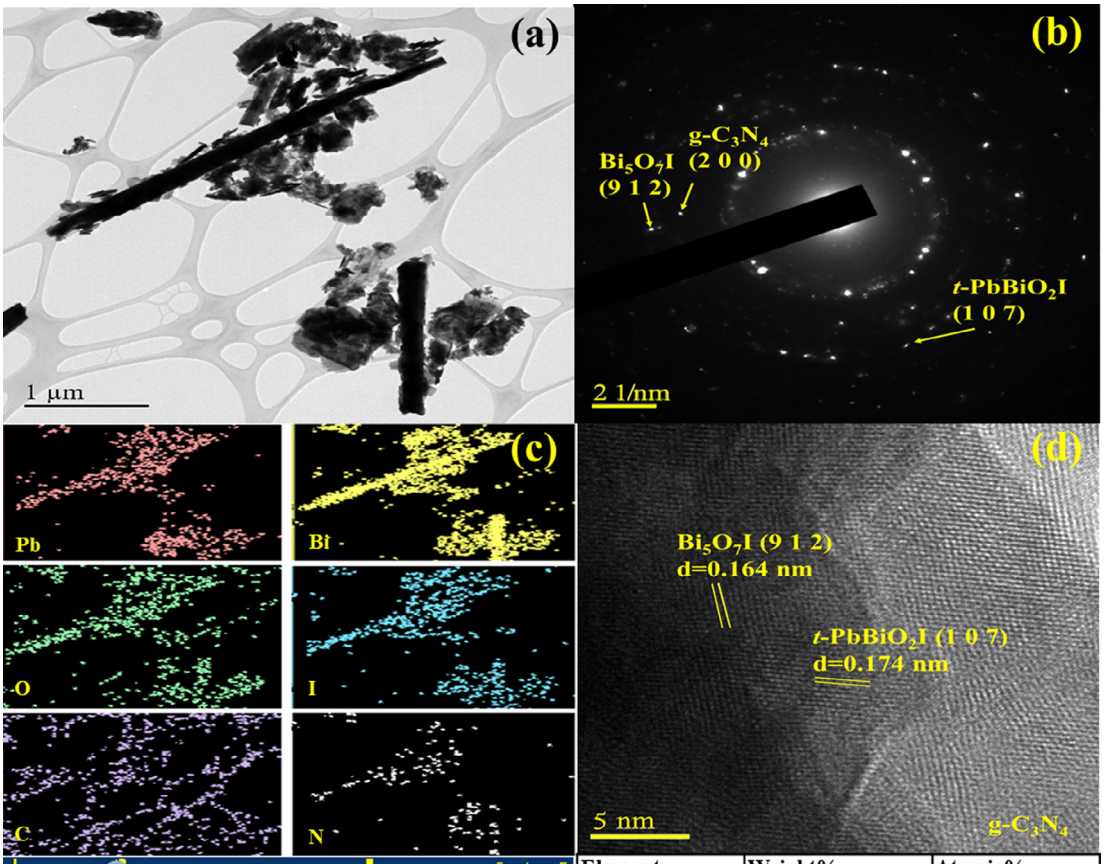

Element	Weight%	Atomic%
C K	4.59	30.94
N K	1.55	8.96
O K	4.60	23.25
I L	8.67	5.53
Pb L	27.34	10.68
Bi L	53.25	20.63
Totals	100.00	

(f)

Fig. 2. (a) FE-TEM images, (b) SAD, (c) mapping, (d) HR-image, and (e) (f) EDS of *t*-$PbBiO_2I$/Bi_5O_7I/g-C_3N_4 (B3PI-1%C3N4-13–100-12) samples by the hydrothermal autoclave method.

variations in the Pb peak binding energy; in addition, they reported the peak's relative integral intensity to be based on the particle fraction in the specific region [11], signifying that greater successive ionic layer adsorption and reaction cycles engendered the creation of a fraction of bigger particles and smaller particles on the titania nanotube surface. The two different Pb^{2+} phases created in the derived composites can be attributed to the $4f_{7/2}$ peaks that were determined at 137.2 and 138.2 eV. Fig. 3(c) two reveals the spectra derived for Bi 4f to be deconvoluted into two peaks at 158.3- and 159.9-eV binding energies ascribed to Bi $4f_{7/2}$, which were also determined to be attributable to Bi existing in a trivalent oxidation state. Two different Bi^{3+} phases within the $PbBiO_2I$/Bi_5O_7I/g-C_3N_4 composites can explain these $4f_{7/2}$ peaks. Chen et al. [31] also indicated a comparable chemical binding observation for Bi $4f_{7/2}$. Furthermore, the asymmetric peak derived from the O 1s spectra shown in Fig. 3(d) could be decomposed using a program for XPS peak fitting, yielding two O 1s peaks at 529.7 and 531.2 eV, which were determined to correspond to *t*-$PbBiO_2I$ and Bi_5O_7I lattice oxygen atoms [24]. The peaks observed at 619.4- and 618.5-eV binding energies, as shown in Fig. 3(e), were determined to correspond to I $3d_{5/2}$, and this was ascribed to I existing in the monovalent oxidation state for Bi_5O_7I and *t*-$PbBiO_2I$. Fig. 3(f) illustrates the composites' HR C 1s spectra, demonstrating primarily two carbon species: sp^2 C—C bonds (284.5 eV) and sp^2-hybridized carbon that was determined to exist in the aromatic ring containing N (N—C=N) (287.8 eV). A study demonstrated the latter to be the primary species in polymeric g-C_3N_4 [32]. As illustrated in Fig. 3(q), the spectra of N1s could be deconvoluted into three peaks at 398.0, 399.4, and 400.8 eV. The highest peak that was centered at 398.0 eV was determined to correspond to sp^2-hybridized N contained in triazine rings (C—N=C), and that noted at 399.4 eV was determined to correspond to the tertiary N—$(C)_3$ groups. Both units, in addition to sp^2-hybridized carbon (N—C=N, 287.8 eV), were determined to constitute the units of heptazine heterocyclic rings, thus forming the fundamental units of the substructure of g-C_3N_4 polymers. Finally, the weak peak that was observed at 400.8 eV was determined to correspond to the effects of charging or to positive charge localization in heterocycles [33]. The presented results were concordant with the XRD and TEM results.

Chen et al. [11,29,31] have demonstrated formation processes associated with a sequence of bismuth oxybromides and lead bismuth oxychlorides. Eqs. (1)–(10) describe the *t*-$PbBiO_2I/Bi_5O_7I$ formation processes proposed by the current study. The compounds that were realized under various hydrothermal conditions were demonstrated to undergo a series of changes, described as $BiOI \rightarrow Bi_4O_5I_2 \rightarrow Bi_7O_9I_3 \rightarrow Bi_3O_4I \rightarrow Bi_5O_7I \rightarrow \alpha\text{-}Bi_2O_3$ and $PbI_2 \rightarrow Pb(OH)I \rightarrow PbBiO_2I$. Controlling the hydrothermal reaction's pH yielded various compositions:

$$Bi^{3+} + 3OH^- \rightarrow Bi(OH)_{3(s)} \quad (1)$$

$$12Bi(OH)_{3(s)} + 6HNO_3 \rightarrow 2[Bi_6O_6(OH)_3(NO_3)_3{\cdot}1.5H_2O]_{(s)} + 15H_2O \quad (2)$$

$$5Bi(OH)_{3(s)} + I^- \rightarrow Bi_5O_7I_{(s)} + 7H_2O + OH^- \quad (3)$$

$$Bi^{3+} + 3I^- \rightarrow BiI_{3(s)} \quad (4)$$

$$5BiI_{3(s)} + 14OH^- \rightarrow Bi_5O_7I_{(s)} + 14I^- + 7H_2O \quad (5)$$

$$Pb^{2+} + 2I^- \rightarrow PbI_{2(s)} \quad (6)$$

$$PbI_{2(s)} + OH^- \rightarrow Pb(OH)I_{(s)} \quad (7)$$

$$Pb(OH)I_{(s)} + OH^- \rightarrow Pb(OH)_2 + I^- \quad (8)$$

$$BiOI_{(s)} + Pb(OH)_2 \rightarrow PbBiO_2I_{(s)} + H_2O \quad (9)$$

$$Pb(OH)_2 \rightarrow PbO_{(s)} + H_2O \quad (10)$$

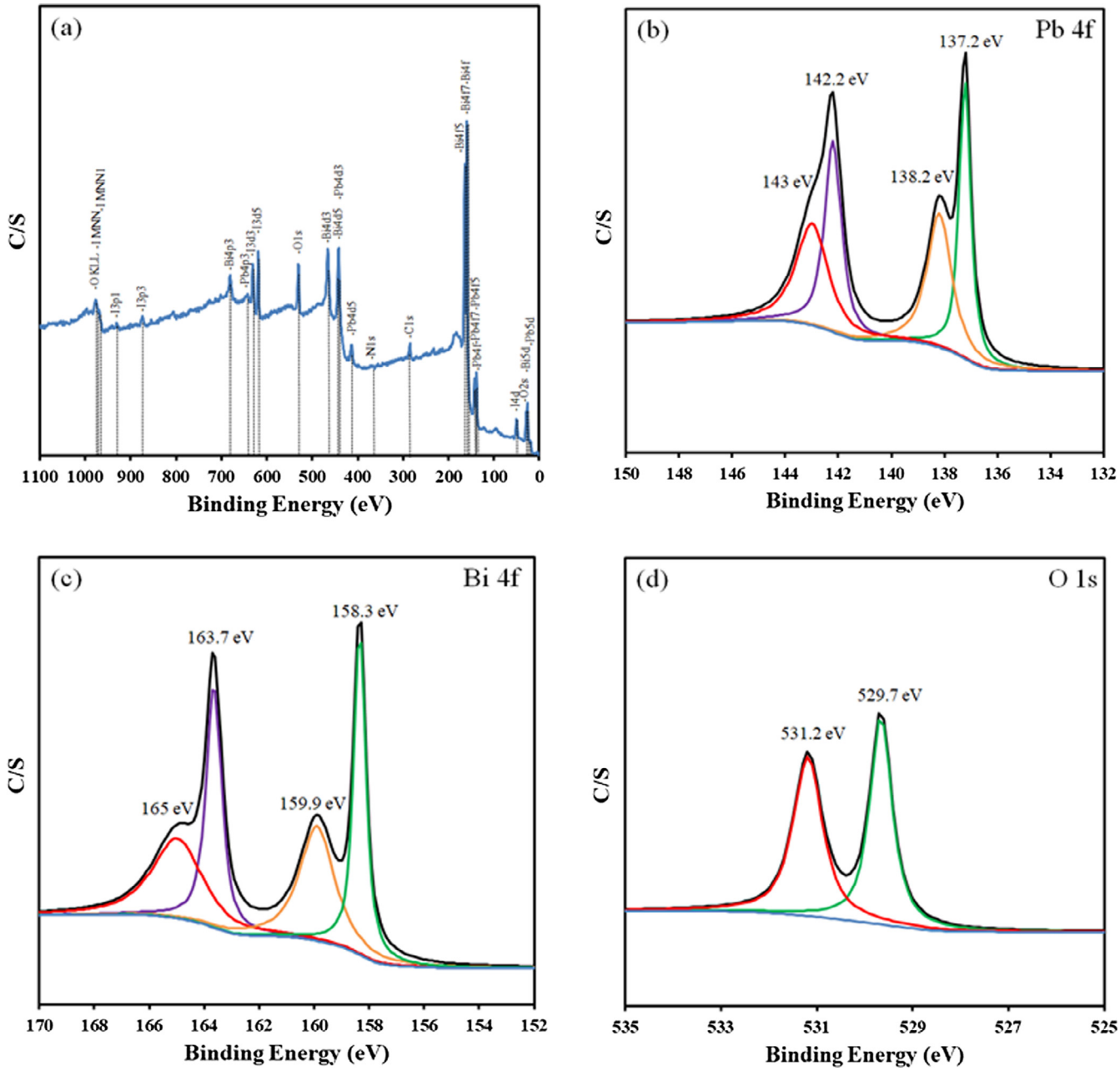

Fig. 3. XPS spectra of *t*-$PbBiO_2I/Bi_5O_7I/g\text{-}C_3N_4$ (B3PI-13-100-12). (a) Total survey, (b) Pb 4f, (c) Bi 4f, (d) O 1s, (e) I 3d, (f) C 1s, and (g) N 1s.

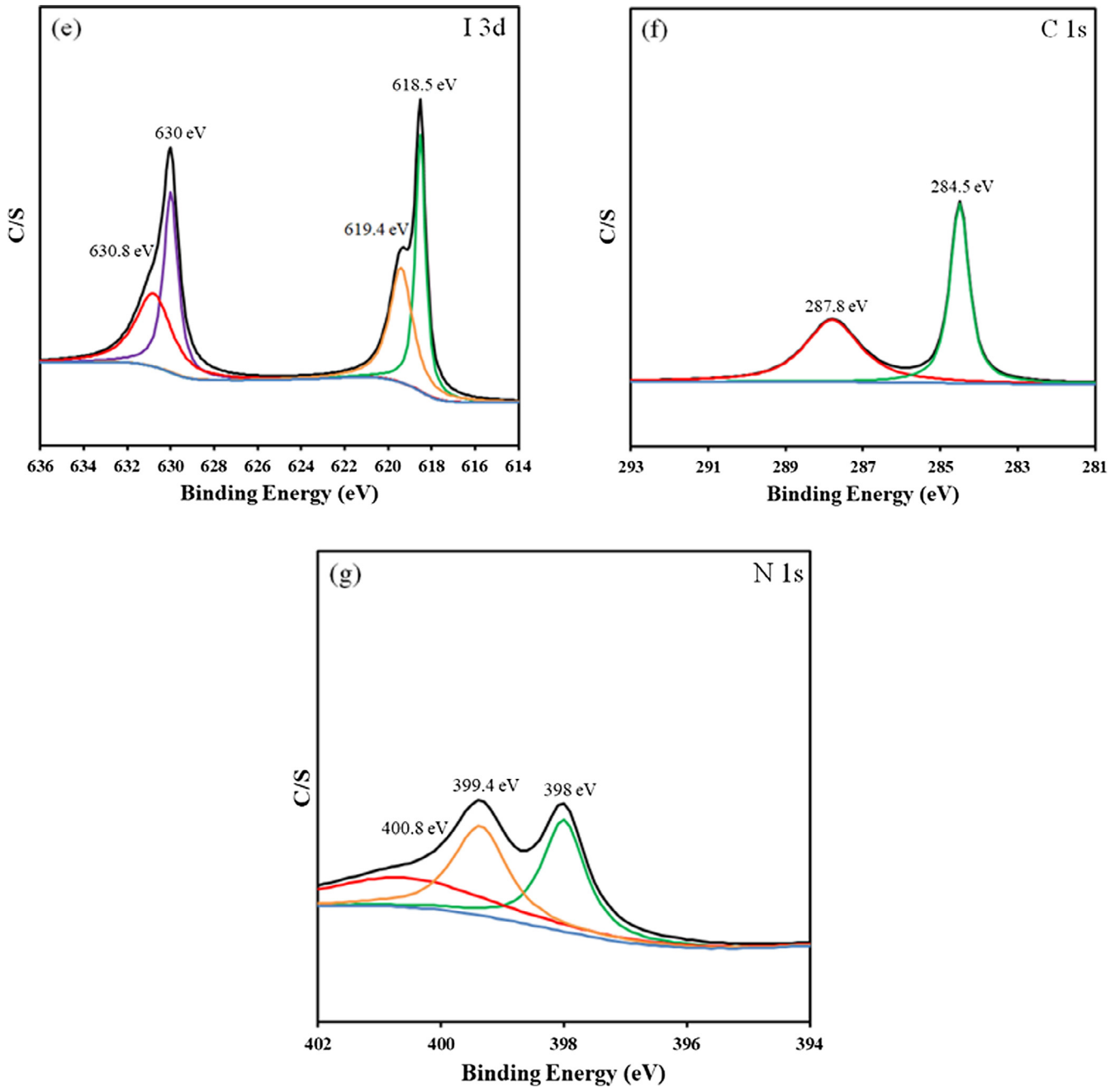

Fig. 3 (*continued*)

3.1.4. Fourier-transform infrared spectroscopy

Fig. 4 presents the *t*-$PbBiO_2I/Bi_5O_7I$/g-C_3N_4 composites' (realized at various weight percentages) Fourier-transform infrared spectroscopy spectra, revealing a strong absorption that is located mainly at 400–900 cm^{-1}; this was noted in this study to correspond to Bi—O, Bi—O—I, Bi—O—Bi, and Pb—O in *t*-$PbBiO_2I/Bi_5O_7I$ stretching vibrations [34]. Concerning pure g-C_3N_4, peaks were observed at 1254, 1328, 1422, 1574, and 1641 cm^{-1}, noted in this study to correspond to the typical stretching modes that are associated with the CN heterocycles [35]. Additionally, the results revealed the breathing mode typical to the triazine units to be located at 813 cm^{-1} [36], an observation determined to be concordant with the XRD- and TEM-derived results. Furthermore, *ν*(C—O) stretching vibrations were noted to be represented by a strong broad band that was located at 1387 cm^{-1}. The (OCO) out-of-plane vibration was indicated to be represented by a medium strong band that was located at approximately 821 cm^{-1}. As manifested by the $PbCO_3{\cdot}nH_2O$ infrared spectra, a portion of the derived products in this study possessed a water molecule that was uncoordinated. As expected, the *ν*(O—H)-stretching-vibration-related band that was associated with uncoordinated H_2O was noted to be existing at approximately 3000 cm^{-1}. As indicated in Fig. 3(b), the spectra derived for Pb 4f were deconvoluted in this study into two peaks at 137.2- and 138.2-eV binding energies that were noted to be attributable to *t*-$PbBiO_2I$ and $PbCO_3$ Pb $4f_{7/2}$, which could be engendered by Pb existing in the divalent oxidation state. The presented results were concordant with the XPS-derived results.

3.1.5. Morphological structure and composition

Fig. 5 depicts the *t*-$PbBiO_2I/Bi_5O_7I$/g-C_3N_4 FE-SEM images; the images derived are depicted at a high level of magnification. The morphologies of *t*-$PbBiO_2I$ were noted to resemble an irregular

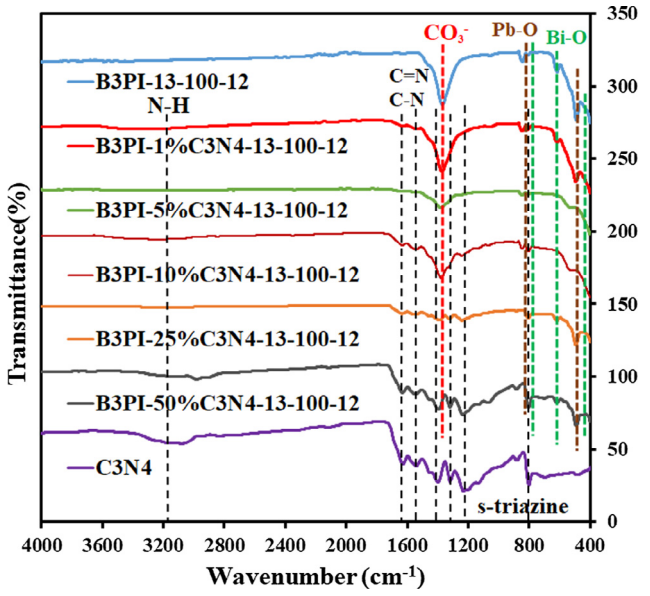

Fig. 4. FT-IR of as-prepared samples under different amount of g-C_3N_4 composite with *t*-$PbBiO_2I/Bi_5O_7I$. (Molar ratio $Pb(NO_3)_2/Bi(NO_3)_3$ = 1/3 mmol/mmol, KI = 1 mmol, reaction temp = 100 °C, reaction time 12 h).

plate [14,17]. The morphologies of Bi_5O_7I were noted to resemble an irregular plate [37]. The morphologies of g-C_3N_4 were noted to resemble an irregular nanosheet [35]. The *t*-$PbBiO_2I/Bi_5O_7I$/g-C_3N_4 samples' morphologies were noted to resemble an irregular plate, long rod, and irregular nanosheet. Pb, Bi, O, I, C, and N mainly constituted the derived samples, as the SEM-EDS results demonstrated. The aforementioned results reveal the controlled hydrothermal method to be effective for realizing selective composite synthesis.

3.1.6. Optical absorption properties

The diffuse-reflectance ultraviolet (UV) results derived for the as-prepared samples revealed the samples' absorption edge to be approximately 466.2–516.7 nm (Fig. 6), which was noted to be engendered by the 2.40–2.66-eV band gap and also to be accordant with reported results [16,37,38]. Only a modest visible light amount is absorbed by pure t-$PbBiO_2I$ and Bi_5O_7I. An $(\alpha h\nu)^{1/2}$ plot against energy ($h\nu$) determined the *t*-$PbBiO_2I/Bi_5O_7I$/g-C_3N_4 E_g value (i.e., 2.40 eV). It can be seen from the figure that the *t*-$PbBiO_2I/Bi_5O_7I$/g-C_3N_4 composite with different g-C_3N_4 contents showed effective light absorption for wavelengths more than 466.2 nm, demonstrating that the *t*-$PbBiO_2I/Bi_5O_7I$/g-C_3N_4 composites are effective visible-light-driven photocatalysts. Moreover, the absorption intensity of the *t*-$PbBiO_2I/Bi_5O_7I$/g-C_3N_4 composites in the entire spectrum is obviously enhanced and the absorption edge of the *t*-$PbBiO_2I/Bi_5O_7I$/g-C_3N_4 composites is significantly red shifted compared to the pure g-C_3N_4. Pure g-C_3N_4 are particles are light yellow powder, and with the introduction of *t*-$PbBiO_2I/Bi_5O_7I$, the *t*-$PbBiO_2I/Bi_5O_7I$/g-C_3N_4 composites gradually become yellow powder, thereby showing enhanced light absorption. The Fig. 6(b) demonstrated the conventional Tauc plot of crystalline *t*-$PbBiO_2I/Bi_5O_7I$, g-C_3N_4, and *t*-$PbBiO_2I/Bi_5O_7I$/g-C_3N_4; the bandgap (2.47 and 2.66 eV) of *t*-$PbBiO_2I/Bi_5O_7I$ and g-C_3N_4 could be easily obtained by extrapolating to the x-axis. The introduction of g-C_3N_4 enhances the ability of *t*-$PbBiO_2I/Bi_5O_7I$ to respond to more visible light to produce more photogenerated carriers and promote its photocatalytic performance.

3.1.7. Adsorption–desorption isotherm and BET

Fig. 7 illustrates the isotherm curves of N adsorption–desorption derived for *t*-$PbBiO_2I/Bi_5O_7I$/g-C_3N_4, *t*-$PbBiO_2I/Bi_5O_7I$, and g-C_3N_4. The *t*-$PbBiO_2I/Bi_5O_7I$/g-C_3N_4 isotherm was noted to approximate Type IV isotherms along with a hysteresis loop observed at a relatively high pressure of 0.6–1.0 [39]. Because such types of self-organized porous architectures afford highly efficient

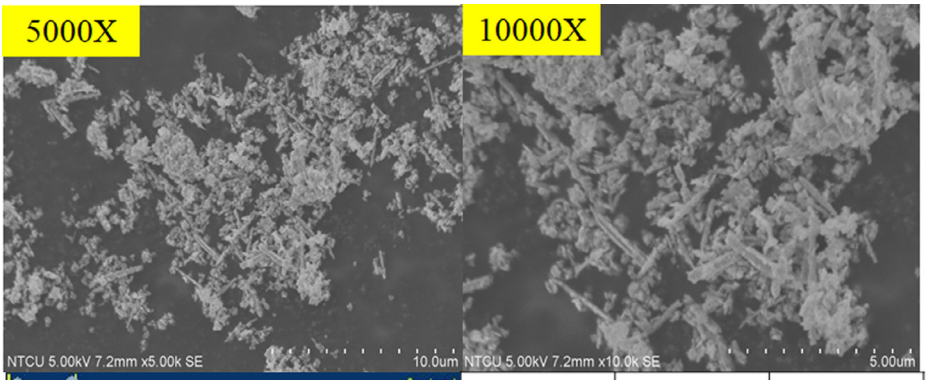

Element	Weight%	Atomic%
C K	23.60	49.19
N K	14.82	26.49
O K	11.37	17.80
I L	6.35	1.25
Pb M	5.99	0.72
Bi M	37.86	4.54
Totals	100.00	

Fig. 5. SEM images of *t*-$PbBiO_2I/Bi_5O_7I$/g-C_3N_4 by the hydrothermal autoclave method. (Molar ratio $Pb(NO_3)_2/Bi(NO_3)_3$ = 1/3, KI = 1 mmol, hydrothermal conditions: pH = 13, temp = 100 °C, time = 12 h).

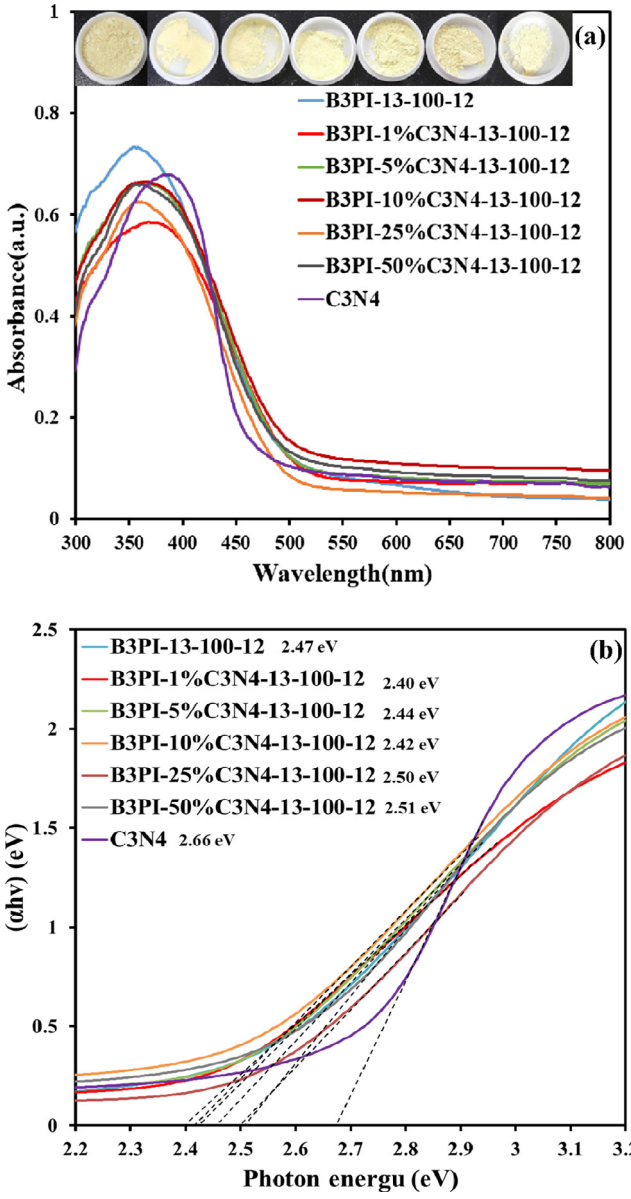

Fig. 6. UV–vis absorption spectra of the as-prepared photocatalysts under different amount of g-C_3N_4 composite with *t*-$PbBiO_2I/Bi_5O_7I$.

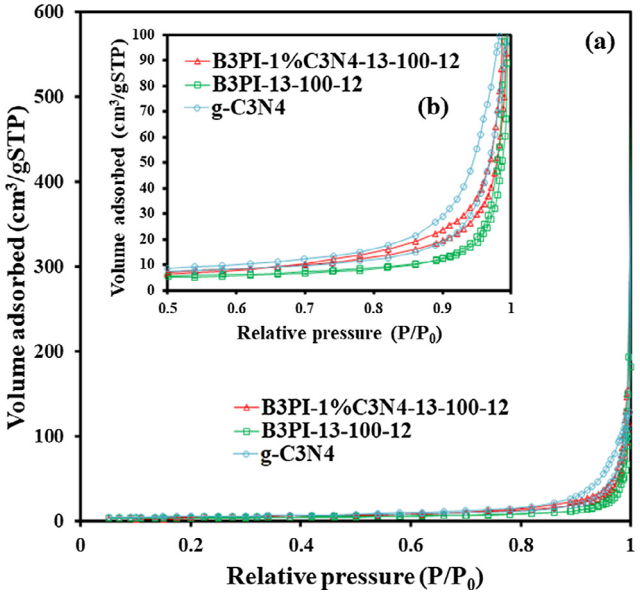

Fig. 7. (a) Nitrogen adsorption-desorption isotherms (inset) and (b) the corresponding pore size distribution curve for *t*-$PbBiO_2I/Bi_5O_7I$/g-C_3N_4, *t*-$PbBiO_2I/Bi_5O_7I$, and g-C_3N_4.

pathways for the reactant and product molecule transport, they are determined to be remarkably valuable in photocatalysis [40]. From Table 3, the *t*-$PbBiO_2I/Bi_5O_7I$/g-C_3N_4, *t*-$PbBiO_2I/Bi_5O_7I$, g-C_3N_4 samples had S_{BET} values of 17.14, 13.47, and 18.44 m^2/g. The pore volume and diameter of *t*-$PbBiO_2I/Bi_5O_7I$/g-C_3N_4 were 0.186 cm^3/g and 348.2 nm, respectively.

3.2. Photocatalytic activity

Fig. 8 reveals the variations observed for the UV–visible spectra in the course CV and HBA photodegradation in the aqueous *t*-$PbBiO_2I/Bi_5O_7I$/g-C_3N_4 dispersions under irradiation that was provided by visible light. We noted approximately 95% of CV to be degraded after 24 h of the mentioned irradiation and approximately 96% of HBA after 12 h.

The derived degradation efficiency as a reaction time function is presented in Fig. 9 and Figs. S3 and S4; applying the as-prepared samples engendered a significant removal efficiency enhancement. In the absence of photocatalysts, CV could not be degraded under visible light irradiation. After 16-h irradiation, the *t*-$PbBiO_2I/Bi_5O_7I$/g-C_3N_4 photocatalytic performance exceeded those of the other samples, with the CV dye elimination efficiency being up to 99%. For the derivation of a clearer comprehension regarding the CV dye degradation reaction kinetics, this study executed an apparent pseudo-first-order model [41] in the experiments, namely $\ln(C_o/C) = kt$. The data that are indicated in Table 4 and Table S4 were subjected to a first-order linear fit; accordingly, the *t*-$PbBiO_2I/Bi_5O_7I$/g-C_3N_4 (B3PI-1%C3N4-13-100-12) k value was derived as 3.518×10^{-1} h^{-1} (the maximum degradation rate), a derivation considerably exceeding the derivations for the other composites; the *t*-$PbBiO_2I/Bi_5O_7I$/g-C_3N_4 (B3PI-1%C3N4-13-100-12) photocatalyst realized in this study was noted to have a considerably greater level of effectiveness, compared with the other composites. The superior photocatalytic activity of *t*-$PbBiO_2I/Bi_5O_7I$/g-C_3N_4 (B3PI-1%C3N4-13-100-12) composites might be attributed to its efficient usage of visible light and the high separation efficiency of the electron-hole pairs with its hieratical structure. The *t*-$PbBiO_2I/Bi_5O_7I$/g-C_3N_4 (B3PI-1%C3N4-13-100-12) composite with a large S_{BET} did exhibit the highest photocatalytic ability among all the samples, suggesting that changes in the photocatalytic ability were associated with the BET surface area, its efficient use of visible-light, and the highly effective separation of electron–hole pairs within its samples. To execute a durability evaluation for the *t*-$PbBiO_2I/Bi_5O_7I$/g-C_3N_4 composite, this study recycled the previously used catalyst. Through the application of centrifugation, the catalyst was collected after each cycle. After the removal of CV in the fourth cycle, the study did not observe any apparent deficit in photocatalytic activity, and the determined deficit was 1.5% in the course of the fifth run (Fig. 10(a)). After probing the previously used *t*-$PbBiO_2I/Bi_5O_7I$/g-C_3N_4 through XRD, the study determined no difference between this previously used sample and the as-prepared sample (Fig. 10(b); hence, the derived *t*-$PbBiO_2I/Bi_5O_7I$/g-C_3N_4 composite has good photostability.

For exploring the photogenerated electron–hole pair rate of recombination, the current study utilized photoluminescence (PL) spectra. Furthermore, for probing the photogenerated carrier segregation capacity in the heterostructures, the study employed *t*-$PbBiO_2I/Bi_5O_7I$/g-C_3N_4 PL spectra (Fig. 11). The results demonstrated a strong emission peak derived for the as-prepared samples

Table 3
Physical and chemical properties of as-prepared samples at different conditions (Pb$(NO_3)_2$/Bi$(NO_3)_2$ = 1/3, pH = 13, temp = 100 °C, time = 12 h).

Samples	S_{BET} ($m^2\ g^{-1}$)	Pore volume ($cm^3\ g^{-1}$)	Pore diameter (nm)	Band gap (eV)
B3PI-13-100-12	13.4705	0.165003	496.773	2.47
B3PI-1%C3N4-13-100-12	17.1418	0.186470	348.2095	2.40
g-C_3N_4	18.4363	0.176410	318.347	2.66

at approximately 460 nm, which was noted to be engendered by the band transitions' direct electron–hole recombination. Nevertheless, the innate emission peak observed for *t*-$PbBiO_2I/Bi_5O_7I$/g-C_3N_4 was approximately 460 nm (lowest intensity); the derived result signifies considerable inhibition of photogenerated charge carrier recombination. Efficient segregation of charge could engender prolongation of the charge carrier lifetime and the

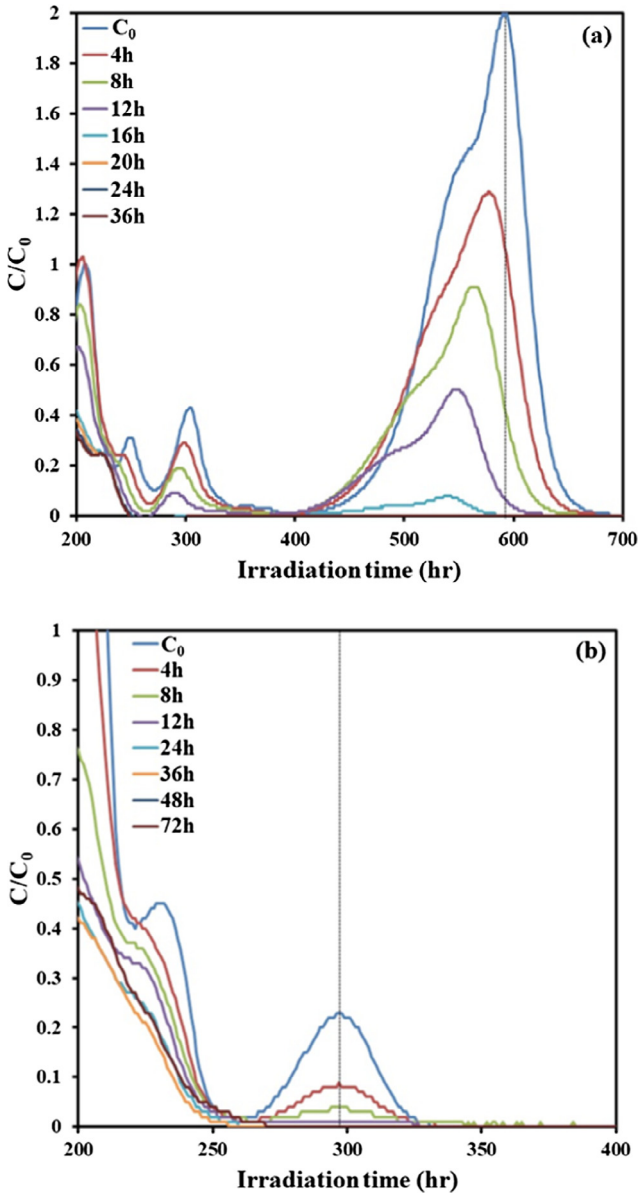

Fig. 8. Temporal UV–vis adsorption spectral changes during the photocatalytic degradation of (a) CV and (b) HBA over aqueous *t*-$PbBiO_2I/Bi_5O_7I$/g-C_3N_4 under visible light irradiation.

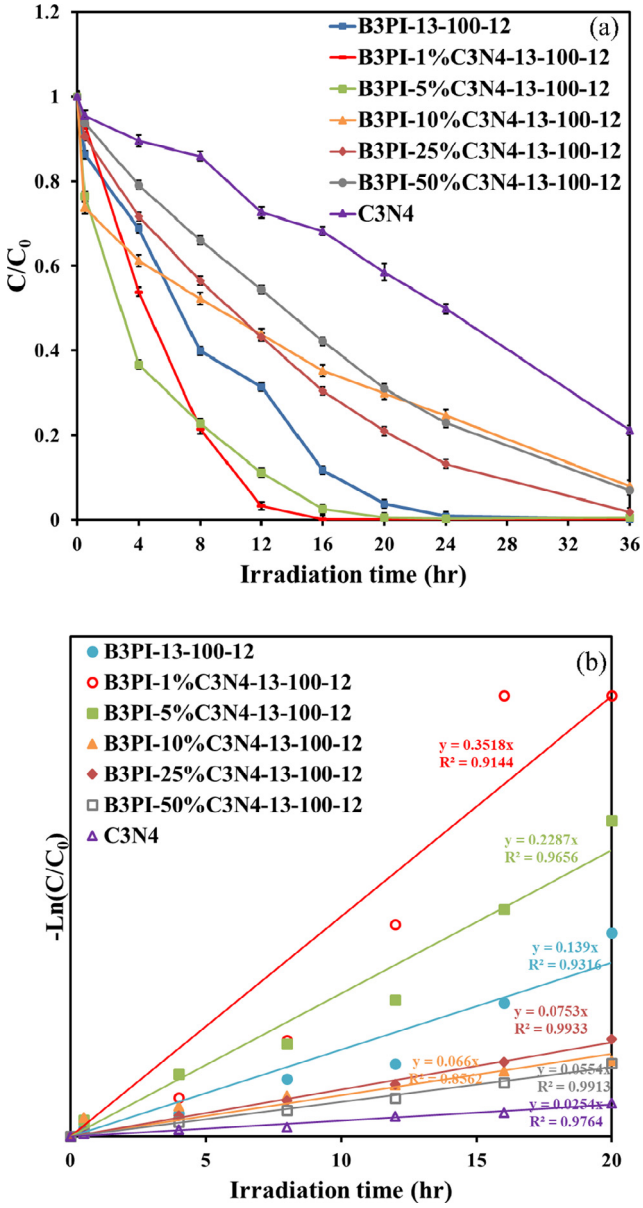

Fig. 9. Photocatalytic activity of as-prepared samples for CV photocatalytic degradation under different g-C_3N_4 amount. (Molar ratio Pb$(NO_3)_2$/Bi$(NO_3)_3$ = 1/3 mmol/mmol, KI = 1 mmol, reaction temp = 100 °C, pH = 13, reaction time = 12 h).

Table 4
Pseudo-first-order rate constant for CV photocatalytic oxidation under different photocatalysts.

Sample	k (h^{-1})	R^2
B3PI-13-100-12	0.2518	0.9795
B3PI-1%C3N4-13-100-12	**0.3518**	0.9144
B3PI-5%C3N4-13-100-12	0.2287	0.9656
B3PI-10%C3N4-13-100-12	0.062	0.8511
B3PI-25%C3N4-13-100-12	0.0753	0.9933
B3PI-50%C3N4-13-100-12	0.0554	0.9913
B3PI-13-150-12	0.1186	0.9705
B3PI-5%C3N4-13-150-12	0.0661	0.9533
B3PI-10%C3N4-13-150-12	0.062	0.8511
B3PI-25%C3N4-13-150-12	0.1616	0.9708
B3PI-50%C3N4-13-150-12	***0.1877***	0.967
B3P3I-4-100-12	0.0813	0.8147
B3P3I-5%C3N4-4-100-12	0.0813	0.8539
B3P3I-10%C3N4-4-100-12	0.0549	0.9636
B3P3I-25%C3N4-4-100-12	***0.1427***	0.9624
B3P3I-50%C3N4-4-100-12	0.071	0.9609

Table 4 (*continued*)

Sample	k (h^{-1})	R^2
B3P3I-4-150-12	0.0957	0.8994
B3P3I-5%C3N4-4-150-12	0.0145	0.1391
B3P3I-10%C3N4-4-150-12	0.0185	0.4757
B3P3I-25%C3N4-4-150-12	***0.1477***	0.9645
B3P3I-50%C3N4-4-150-12	0.0562	0.9669
B3P5I-4-100-12	0.0474	0.6918
B3P5I-5%C3N4-4-100-12	0.1271	0.9834
B3P5I-10%C3N4-4-100-12	***0.1365***	0.9764
B3P5I-25%C3N4-4-100-12	0.0188	0.8445
B3P5I-50%C3N4-4-100-12	0.0152	0.8677
B3P5I-4-150-12	0.105	0.9758
B3P5I-5%C3N4-4-150-12	***0.1663***	0.9573
B3P5I-10%C3N4-4-150-12	0.0326	0.9623
B3P5I-25%C3N4-4-150-12	0.0471	0.9524
B3P5I-50%C3N4-4-150-12	0.0441	0.9669
C3N4	0.0254	0.9764

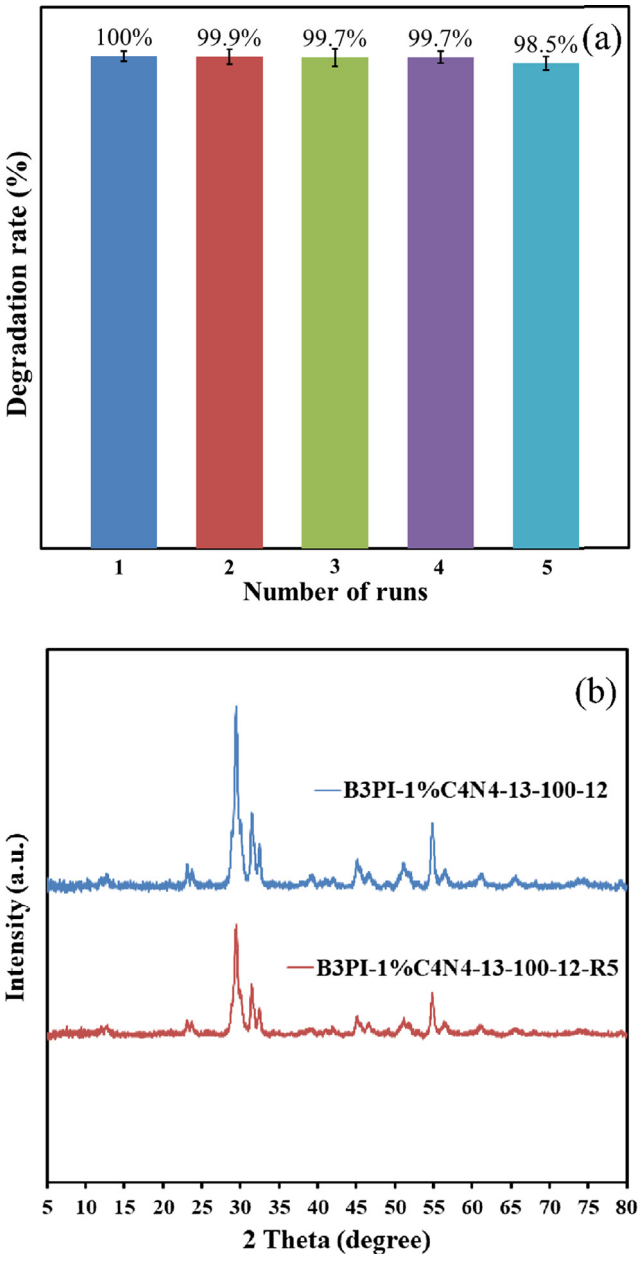

Fig. 10. (a) Cycling runs and (b) XRD patterns acquired before and after the photocatalytic degradation of CV in the presence of *t*-$PbBiO_2I/Bi_5O_7I/g\text{-}C_3N_4$ (B3PI-1%C3N4-13-100-12).

augmentation of interfacial charge transfer efficiency to the adsorbed substrates, consequently inducing photocatalytic activity augmentation. The *t*-$PbBiO_2I/Bi_5O_7I/g\text{-}C_3N_4$ heterojunctions' observed photocatalytic activity reached 0.3518 h^{-1} (the maximum rate constant), exceeding the values that were derived for the photocatalysts *t*-$PbBiO_2I$, Bi_5O_7I, g-C_3N_4, and *t*-$PbBiO_2I/Bi_5O_7I$ by 15, 6.6, 13.1, and 1.4 times, respectively. The derived results consequently suggest the *t*-$PbBiO_2I/Bi_5O_7I/g\text{-}C_3N_4$ heterojunctions to be integral in photocatalytic activity augmentation. The preceding PL results derived in this study thus confirm the composites' significance in obstructing electron–hole recombination and also explain the *t*-$PbBiO_2I/Bi_5O_7I/g\text{-}C_3N_4$ composites' increased photocatalytic performance.

3.3. CV photodegradation mechanism

For evaluating the influence engendered by active species during photocatalytic reaction courses, the study introduced diverse quenchers so as to scavenge the appropriate active species [42]. Introducing the BQ quencher reduced the CV dye photocatalytic degradation (Fig. 12) when compared with that executed without quencher introduction, consequently signifying $O_2^{\cdot-}$ to serve as the major active species in the CV dye photocatalytic degradation mechanism of CV.

The results obtained from the executed structural characterizations demonstrate the *t*-$PbBiO_2I/Bi_5O_7I/g\text{-}C_3N_4$ photocatalyst to be a three-phase composite. The noted photocatalytic activity of the derived composite considerably exceeded the determined activity of the component phase alone; hence, the assumption of possible synergistic effects between *t*-$PbBiO_2I/Bi_5O_7I$ and g-C_3N_4 is reasonable. Actually, numerous researchers have indicated the existence of synergistic effects in composites comprising two semiconductors that are in contact [43,44], with the noted effects being ascribed to efficient charge transfer achieved at the two semiconductors' interface; the described phenomenon could engender photoexcited electron–hole segregation effectiveness and, as a result, photocatalytic activity augmentation. The charge transfer process is motivated by the correspondence of band potentials. An appropriate band potential thus constitutes the precondition associated with the composite photocatalyst synergetic effects.

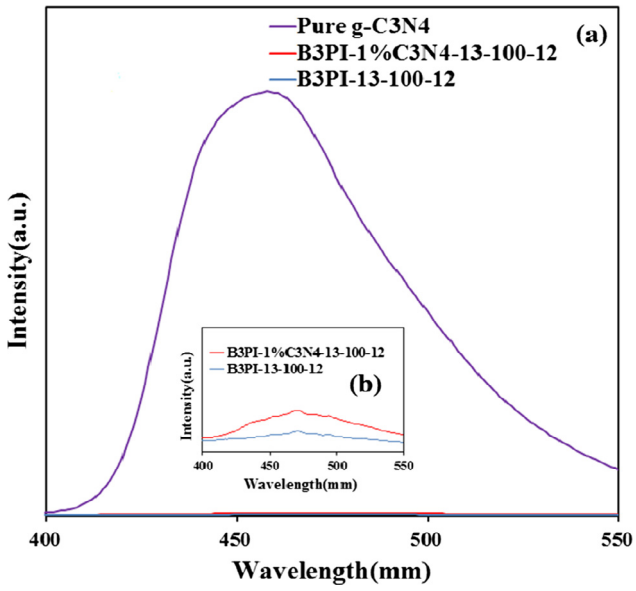

Fig. 11. Photoluminescence (PL) spectra of the *t*-$PbBiO_2I/Bi_5O_7I/g\text{-}C_3N_4$, *t*-$PbBiO_2I/Bi_5O_7I$, and g-$C_3N_4$.

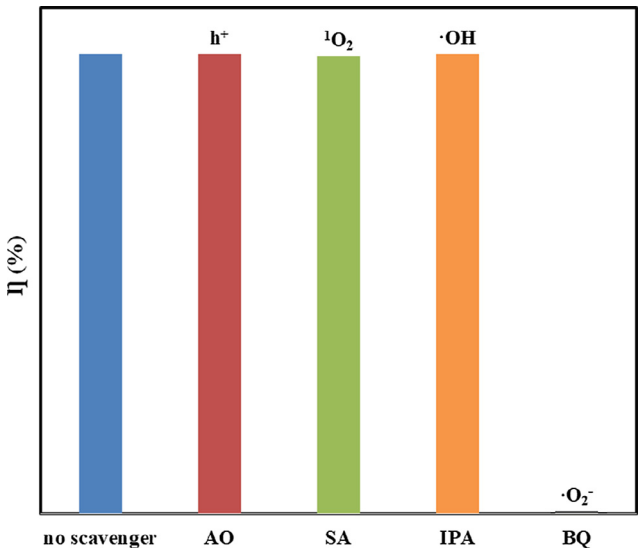

Fig. 12. Photodegradation of CV dye *t*-$PbBiO_2I/Bi_5O_7I/g\text{-}C_3N_4$ in the presence of different scavengers under solar light irradiation.

Fig. 13 presents the band alignment derived for a type-II heterostructure [45] and VB XPS spectra derived for *t*-$PbBiO_2I$, Bi_5O_7I, and g-C_3N_4. The CB and VB positions observed for the g-C_3N_4 semiconductor were noted to be higher than those determined for the *t*-$PbBiO_2I$ and Bi_5O_7I semiconductors, with the CB and VB steps being in the same direction (Fig. 13). The VB edge noted for g-C_3N_4 was at approximately 1.58 eV, concordant with the position noted by Li et al. [45]. Regarding *t*-$PbBiO_2I$ and Bi_5O_7I, the derived VB edges were at 1.83 and 1.77 eV. Therefore, band potentials derived for *t*-$PbBiO_2I$, Bi_5O_7I, and g-C_3N_4 are demonstrated to be suitable. Photoinduced electrons existing on the g-C_3N_4 sample's surface could be transferred conveniently to Bi_5O_7I and subsequently transferred to *t*-$PbBiO_2I$, all occurring through the interfaces; similarly, the holes existing on the *t*-$PbBiO_2I$ sample's surface could migrate to Bi_5O_7I and subsequently migrate to g-C_3N_4. The observed charge transfer was thus noted to be effective in obstructing electron–hole recombination in the two semiconductors, consequently engendering photocatalytic efficiency augmentation.

Fig. 13 details the dye degradation mechanism that is based on the experimental results described in the preceding paragraphs. Immediately after an electron arrives at the *t*-$PbBiO_2I/Bi_5O_7I/g\text{-}C_3N_4$ conduction band, it prompts active oxygen species creation, engendering CV dye degradation. Clearly, in addition to the CV dye photodegradation executed through the routes of *t*-$PbBiO_2I/Bi_5O_7I/g\text{-}C_3N_4$-mediated and photosensitized processes, another route explains the photocatalytic activity augmentation. Photosensitized and photocatalytic processes are both executed in tandem (Fig. 13). Nonetheless, under conditions associated with photosensitized and photocatalytic reactions, electrons that are photogenerated and photosensitized react with photocatalyst-surface-existing oxygen, thus yielding O_2^- radicals; furthermore, O_2^- radicals undergo a reaction with H^+ ions and h^+ holes undergo a reaction with OH^- ions (or H_2O) to yield ·OH radicals. These cycles are sustained when irradiation that is provided by visible light is applied to the system [46]; once many photooxidation cycles are exhausted, Eqs. (11) and (12) can describe the CV dye degradation engendered by the oxidant species yielded.

$$CV + O_2^{-}\cdot/\cdot OH \rightarrow \text{degraded compounds} \quad (11)$$

$$CV^{+}\cdot + O_2^{-}\cdot/\cdot OH \rightarrow \text{degraded compounds} \quad (12)$$

A study noted hydroxylated compounds for photocatalytic CV dye degradation in a semiconductor system galvanized by visible light [46]. Previous reports [24,29,39] have demonstrated *N*-centered radical production to precede *N*-de-alkylation and carbon-centered radical production to precede dye chromophore structure demolition in the operation of CV dye photocatalytic

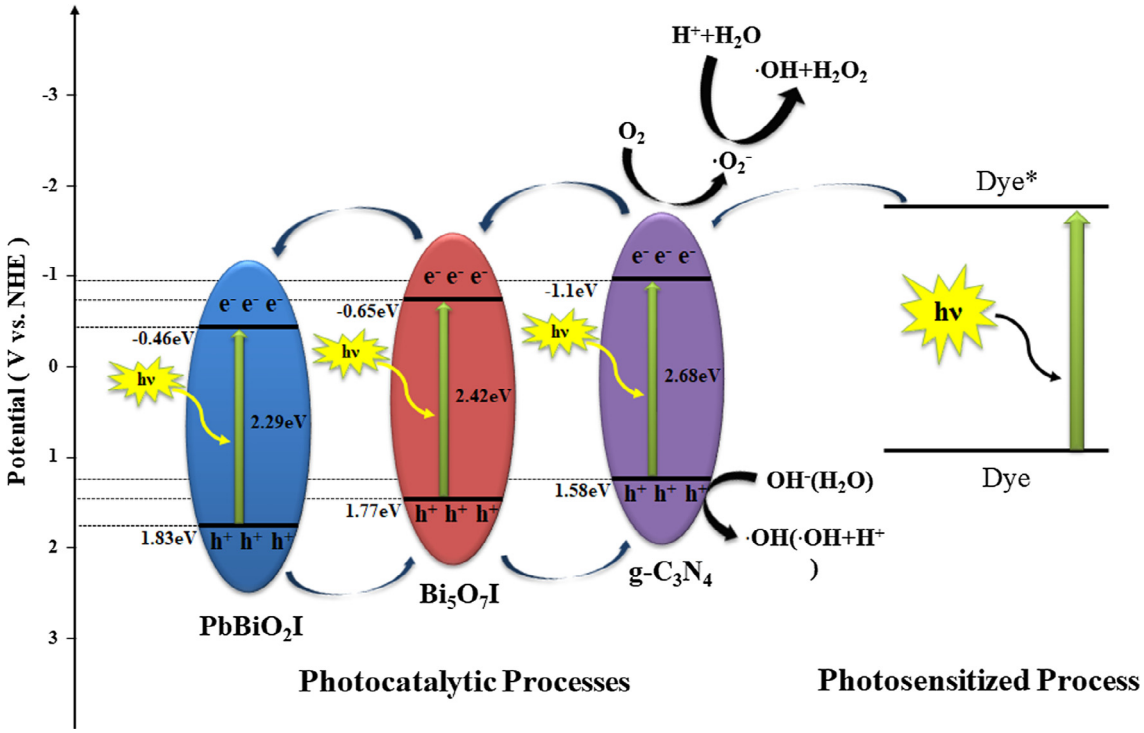

Fig. 13. The band structure diagram of *t*-$PbBiO_2I/Bi_5O_7I/g\text{-}C_3N_4$ and the possible charge separation processes.

degradation under irradiation provided by UV or visible light. The derived reaction mechanisms of the proposed *t*-$PbBiO_2I/Bi_5O_7I/g\text{-}C_3N_4$-supported photocatalytic processes can provide a reference regarding dye-decoloration-relevant applications.

4. Conclusions

Template-free hydrothermal methods were realized in this study to synthesize *t*-$PbBiO_2I/Bi_5O_7I/g\text{-}C_3N_4$ heterojunctions. Using *t*-$PbBiO_2I/Bi_5O_7I/g\text{-}C_3N_4$ engendered a significant removal efficiency enhancement. Catalytic performance observation revealed that using *t*-$PbBiO_2I/Bi_5O_7I/g\text{-}C_3N_4$ resulted in an optimal reaction rate constant of 0.3518 h^{-1}, a derivation exceeding the derivations for the photocatalysts *t*-$PbBiO_2I$, Bi_5O_7I, $g\text{-}C_3N_4$, and *t*-$PbBiO_2I/Bi_5O_7I$ by 15, 6.6, 13.1, and 1.4 times, respectively. The *t*-$PbBiO_2I/Bi_5O_7I/g\text{-}C_3N_4$ photocatalytic activity augmentation was noted to correspond to the heterojunction formation between *t*-$PbBiO_2I$, Bi_5O_7I, and $g\text{-}C_3N_4$, an effective phenomenon in obstructing photogenerated electron–hole recombination. The observed heterojunction formation could explain the *t*-$PbBiO_2I/Bi_5O_7I/g\text{-}C_3N_4$ photocatalytic activity enhancement. As demonstrated by the quenching effects that were associated with scavengers, reactive $O_2^{\cdot-}$ executed a major role in the CV dye photocatalytic degradation. The method realized in this study is valuable for *t*-$PbBiO_2I/Bi_5O_7I/g\text{-}C_3N_4$ synthesis and CV dye photocatalytic degradation for future applications in environmental pollution regulation.

Acknowledgments

This research was supported by the Ministry of Science and Technology of the Republic of China (MOST-105-2119-M-142-001).

References

[1] M.R. Hoffmann, S.T. Martin, W. Choi, D.W. Bahnemann, Environmental applications of semiconductor photocatalysis, Chem. Rev. 95 (1995) 69–96.
[2] A. Kubacka, M. Fernández-García, G. Colón, Advanced nanoarchitectures for solar photocatalytic applications, Chem. Rev. 112 (2012) 1555–1614.
[3] S.T. Huang, Y.R. Jiang, S.Y. Chou, Y.M. Dai, C.C. Chen, Synthesis, characterization, photocatalytic activity of visible-light-responsive photocatalysts BiO_xCl_y/BiO_mBr_n by controlled hydrothermal method, J. Mol. Catal. A: Chem. 391 (2014) 105–120.
[4] H. Cheng, B. Huang, Y. Dai, Engineering BiOX (X = Cl, Br, I) nanostructures for highly efficient photocatalytic applications, Nanoscale 6 (2014) 2009–2026.
[5] Z. Chen, H. Jiang, W. Jin, C. Shi, Enhanced photocatalytic performance over $Bi4Ti_3O_{12}$ nanosheets with controllable size and exposed 001 facets for Rhodamine B degradation, Appl. Catal. B: Environ. 180 (2016) 698–706.
[6] J.A. Seabold, K.S. Choi, Efficient and stable photo-oxidation of water by a bismuth vanadate photoanode coupled with an iron oxyhydroxide oxygen evolution catalyst, J. Am. Chem. Soc. 134 (2012) 2186–2192.
[7] W. Wei, Y. Dai, B.B. Huang, First-principles characterization of bi-based photocatalysts: $Bi_{12}TiO_{20}$, $Bi_2Ti_2O_7$, and $Bi_4Ti_3O_{12}$, J. Phys. Chem. C 113 (2009) 5658–5663.
[8] M. Batuk, D. Batuk, A.A. Tsirlin, D.S. Filimonov, Layered oxychlorides $[PbBiO_2]A_{n+1}BnO_{3n-1}Cl_2$ (A = Pb/Bi, B = Fe/Ti): intergrowth of the hematophanite and sillen phases, Chem. Mater. 27 (2015) 2946–2956.
[9] H.P. Lin, W.W. Lee, S.T. Huang, L.W. Chen, T.W. Yeh, J.Y. Fu, C.C. Chen, Controlled hydrothermal synthesis of $PbBiO_2Br/BiOBr$ heterojunction with enhanced visible-driven-light photocatalytic activities, J. Mol. Catal. A: Chem. 417 (2016) 168–183.
[10] Y. Yu, Y. Gu, W. Zheng, Y. Ding, Y. Cao, New type photocatalyst $PbBiO_2Cl$: materials design and experimental validation, J. Phys. Chem. C 119 (2015) 28190–28193.
[11] F.Y. Liu, Y.R. Jiang, C.C. Chen, W.W. Lee, Novel synthesis of $PbBiO_2Cl/BiOCl$ nanocomposite with enhanced visible-driven-light photocatalytic activity, Catal. Today 300 (2018) 112–123.
[12] B. Wang, J. Di, P.F. Zhang, J.X. Xia, S. Dai, H.M. Li, Ionic liquid-induced strategy for porous perovskite-like $PbBiO_2Br$ photocatalysts with enhanced photocatalytic activity and mechanism insight, Appl. Catal. B: Environ. 206 (2017) 127–135.
[13] Sheng Yin, Ting Wu, Ming Li, Jun Di, Mengxia Ji, Bin Wang, Yong Chen, Jiexiang Xia, Huaming Li, Controllable synthesis of perovskite-like $PbBiO_2Cl$ hollow microspheres with enhanced photocatalytic activity for antibiotic removal, CrystEngComm 19 (2017) 4777–4788.
[14] Sheng Yin, Ming Li, Wenmin Fan, Yi Ding, Ting Wu, Jun Di, Mengxia Ji, Jiexiang Xia, Huaming Li, Controlled synthesis of novel $PbBiO_2I$ microsphere structure towards photocatalytic degradation of bisphenol A, Res. Chem. Intermed. (2018), https://doi.org/10.1007/s11164-018-3461-6.
[15] S. Rau, B. Schäfer, D. Gleich, E. Anders, M. Rudolph, M. Friedrich, H. Görls, W. Henry, J.G. Vos, Ein supramolekularer photokatalysator zur erzeugung von wasserstoff und zur selektiven hydrierung von tolan, Angew. Chem. 118 (2006) 6361–6364.
[16] S. Füldner, P. Pohla, H. Bartling, S. Dankesreiter, R. Stadler, M. Gruber, A. Pfitzner, B. König, Selective photocatalytic reductions of nitrobenzene derivatives using $PbBiO_2X$ and blue light, Green Chem. 13 (2011) 640–643.
[17] F.Y. Liu, J.H. Lin, Y.M. Dai, L.W. Chen, S.T. Huang, T.W. Yeh, J.L. Chang, C.C. Chen, Preparation of perovskites $PbBiO_2I/PbO$ exhibiting visible-light photocatalytic activity, Catalysis Today 314 (2018) 28–41.
[18] M. Li, S. Yin, T. Wu, J. Di, M. Ji, B. Wang, Y. Chen, J. Xia, H. Li, Controlled preparation of $MoS_2/PbBiO_2I$ hybrid microspheres with enhanced visible-light photocatalytic behavior, J. Colloid Interface Sci. 517 (2018) 278–287.
[19] B. Wang, J. Di, G. Liu, S. Yin, J. Xia, Q. Zhang, H. Li, Novel mesoporous graphitic carbon nitride modified $PbBiO_2Br$ porous microspheres with enhanced photocatalytic performance, J. Colloid Interface Sci. 507 (2017) 310–322.
[20] Sunfeng Li, Xing Wang, Yanli Xu, Hanbiao Yang, Fengyu Wei, Xueting Liu, The excellent photocatalytic synergism of $PbBiO_2Br/UiO\text{-}66\text{-}NH_2$ composites via multiple coupling effects, RSC Adv. 6 (2016) 89907–89915.
[21] Hai Guo, Cheng-Gang Niu, Xiao-Ju Wen, Lei Zhang, Guang-Ming Zeng, Construction of highly efficient and stable ternary $AgBr/Ag/PbBiO_2Br$ Z-scheme photocatalyst under visible light irradiation: Performance and mechanism insight, J. Colloid and Interface Sci. 513 (2018) 852–865.
[22] X. Li, J. Wang, D. Xu, Z. Sun, Q. Zhao, W. Peng, Y. Li, G. Zhang, F. Zhang, X. Fan, $NbSe_2$ nanosheet supported $PbBiO_2Br$ as a high performance photocatalyst for the visible light-driven asymmetric alkylation of aldehyde, ACS Sustainable Chem. Eng. 3 (2015) 1017–1022.
[23] P. Wang, B. Huang, X. Qin, X. Zhang, Y. Dai, J. Wei, M.H. Whangbo, Ag@AgCl: a highly efficient and stable photocatalyst active under visible light, Angew. Chem. Int. Ed. 47 (2008) 7931–7933.
[24] Y.R. Jiang, H.P. Lin, W.H. Chung, Y.M. Dai, W.Y. Lin, C.C. Chen, Controlled hydrothermal synthesis of BiO_xCl_y/BiO_mI_n composites exhibiting visible-light photocatalytic degradation of crystal violet, J. Hazard. Mater. 283 (2015) 787–805.
[25] L.S. Zhang, K.H. Wong, H.Y. Yip, C. Hu, J.C. Yu, C.Y. Chan, P.K. Wong, Effective photocatalytic disinfection of *E. coli* K-12 using $AgBr–Ag–Bi_2WO_6$ nanojunction system irradiated by visible light: the role of diffusing hydroxyl radicals, Environ. Sci. Technol. 44 (2010) 1392–1398.
[26] M.C. Yin, Z.S. Li, J.H. Kou, Z.G. Zou, Mechanism investigation of visible light-induced degradation in a heterogeneous TiO_2/Eosin Y/rhodamine B system, Environ. Sci. Technol. 43 (2009) 8361–8366.
[27] S.G. Meng, D.Z. Li, M. Sun, W.J. Li, J.X. Wang, J. Chen, X.Z. Fu, G.C. Xiao, Sonochemical synthesis, characterization and photocatalytic properties of a novel cube-shaped $CaSn(OH)_6$, Catal. Commun. 12 (2011) 972–975.
[28] G. Li, K.H. Wong, X. Zhang, C. Hu, J.C. Yu, R.C.Y. Chan, P.K. Wong, Degradation of acid orange 7 using magnetic AgBr under visible light: the roles of oxidizing species, Chemosphere 76 (2009) 1185–1191.
[29] Y.R. Jiang, S.Y. Chou, J.L. Chang, S.T. Huang, H.P. Lin, C.C. Chen, Hydrothermal synthesis of bismuth oxybromide-bismuth oxyiodide composites with highly visible light photocatalytic performance for the degradation of CV and phenol, RSC Adv. 5 (2015) 30851–30860.
[30] M.M. Rahman, K.M. Krishna, T. Soga, T. Jimbo, M. Umeno, Optical properties and X-ray photoelectron spectroscopic study of pure and Pb-doped TiO_2 thin films, J. Phys. Chem. Solid 60 (1999) 201–210.
[31] H.L. Chen, W.W. Lee, W.H. Chung, H.P. Lin, Y.J. Chen, Y.R. Jiang, W.Y. Lin, C. C. Chen, Controlled hydrothermal synthesis of bismuth oxybromides and their photocatalytic properties, J. Taiwan Inst. Chem. Eng. 45 (2014) 1892–1909.
[32] Y. Li, H. Zhang, P. Liu, D. Wang, Y. Li, H. Zhao, Cross-linked $g\text{-}C_3N_4$/rGO nanocomposites with tunable band structure and enhanced visible light photocatalytic activity, Small 9 (2013) 3336–3344.
[33] J. Zhang, M. Zhang, G. Zhang, X. Wang, Harnessing protein symmetry for enzyme design, ACS Catal. 2 (2012) 940–948.
[34] S.Y. Chou, W.H. Chung, L.W. Chen, Y.M. Dai, W.Y. Lin, J.H. Lin, C.C. Chen, A series of BiO_xI_y/GO photocatalysts: synthesis, characterization, activity, and mechanism, RSC Adv. 6 (2016) 82743–82758.
[35] S.C. Yan, Z.S. Li, Z.G. Zou, Photodegradation performance of $g\text{-}C_3N_4$ fabricated by directly heating melamine, Langmuir 25 (2009) 10397–10401.
[36] J. Zhang, M. Zhang, G. Zhang, X. Wang, Synthesis of carbon nitride semiconductors in sulfur flux for waterphotoredox catalysis, ACS Catal. 2 (2012) 940–948.
[37] W.W. Lee, C.S. Lu, C.W. Chuang, Y.J. Chen, J.Y. Fu, C.W. Siao, C.C. Chen, Synthesis of bismuth oxyiodides and their composites: characterization, photocatalytic activity, and degradation mechanisms, RSC Adv. 5 (2015) 23450–23463.
[38] B.P. Barbero, L.E. Cadus, $V_2O_5–SmVO_4$ mechanical mixture: oxidative dehydrogenation of propane, Appl. Catal. A 237 (2002) 263–273.
[39] H.J. Fan, C.S. Lu, W.L.W. Lee, M.R. Chiou, C.C. Chen, Mechanistic pathways differences between P25-TiO_2 and Pt-TiO_2 mediated CV photodegradation, J. Hazard. Mater. 185 (2011) 227–235.
[40] F. Dong, Y. Sun, M. Fu, Z. Wu, S.C. Lee, Room temperature synthesis and highly enhanced visible light photocatalytic activity of porous BiOI/BiOCl composites nanoplates microflowers, J. Hazard. Mater. 219–220 (2012) 26–34.

[41] A. Chatzitakis, C. Berberidou, I. Paspaltsis, G. Kyriakou, T. Sklaviadis, I. Poulios, Photocatalytic degradation and drug activity reduction of Chloramphenicol, Water Res. 42 (2008) 386–394.
[42] N.M. Dimitrijevic, B.K. Vijayan, O.G. Poluektov, T. Rajh, K.A. Gray, H. He, P. Zapol, Role of water and carbonates in photocatalytic transformation of CO_2 to CH_4 on titania, J. Am. Chem. Soc. 133 (2011) 3964–3971.
[43] H. Li, Y. Zhou, W. Tu, J. Ye, Z. Zou, State-of-the-art progress in diverse heterostructured photocatalysts toward promoting photocatalytic performance, Adv. Funct. Mater. 25 (2015) 998–1013.
[44] Z. Li, J. Feng, S. Yan, Z. Zou, Solar fuel production: Strategies and new opportunities with nanostructures, Nano Today 10 (2015) 468–486.
[45] H. Falcón, J.A. Barbero, J.A. Alonso, M.J. Martínez-Lope, J.L.G. Fierro, $SrFeO_{3-\delta}$ perovskite oxides: chemical features and performance for methane combustion, Chem. Mater. 14 (2002) 2325–2333.
[46] Y. Tian, B. Chang, J. Lu, J. Fu, F. Xi, X. Dong, Hydrothermal synthesis of graphitic carbon nitride–Bi_2WO_6 heterojunctions with enhanced visible light photocatalytic activities, ACS Appl. Mater. Interfaces 5 (2013) 7079–7085.